Radboud Repository

Radboud University Nijmegen

PDF hosted at the Radboud Repository of the Radboud University Nijmegen

The following full text is an author's version which may differ from the publisher's version.

For additional information about this publication click this link.
http://hdl.handle.net/2066/111521

Importance of correlation effects in hcp iron revealed by a pressure-induced electronic topological transition

K. Glazyrin[1,2], L.V. Pourovskii[3,4], L. Dubrovinsky[1], O. Narygina[5], C. McCammon[1],

B. Hewener[6], V. Schünemann[6], J. Wolny[6], K. Muffler[6], A. I. Chumakov[7], W. Crichton[7],

M. Hanfland[7], V. Prakapenka[8], F. Tasnádi[9], M. Ekholm[3], , M. Aichhorn[10], V. Vildosola[11],

A. V. Ruban[12], M. I. Katsnelson[13], I. A. Abrikosov[9]

[1] *Bayerisches Geoinstitut, Universität Bayreuth, 95440 Bayreuth, Germany,*

[2]*Yale University, 06511 New Haven, CT, USA*

[3]*Swedish e-science Research Center (SeRC), Department of Physics, Chemistry and Biology (IFM),*
Linköping University, Linköping, Sweden

[4¶]*Center de Physique Theorique, Ecole Polytechnique, 91128 Palaiseau Cedex, France*

[5]*School of Physics and Astronomy, University of Edinburgh, Edinburgh, UK*

[6]*Technische Universität Kaiserslautern, Kaiserslautern, Germany*

[7]*ESRF, F-38043 Grenoble Cedex, France*

[8]*GeoSoilEnviroCARS, University of Chicago, Argonne National Laboratory, Argonne, IL 60439, USA*

[9]*Department of Physics, Chemistry and Biology (IFM), Linköping University, Linköping, Sweden*

[10]*Institute of theoretical and computational physics, TU Graz, 8010 Graz, Austria*

[11]*Centro Atómico Constituyentes, GIyANN, CNEA, San Martin, Buenos Aires, Comisión Nacional de*
Investigaciones Científicas y Técnicas, Ciudad de Buenos Aires, Argentina

[12]*Department of Materials Science and Engineering, Royal Institute of Technology, SE-10044, Stockholm,*
Sweden

[13]*Radboud University Nijmegen, Institute for Molecules and Materials, 6525 AJ, Nijmegen, Netherlands*

Abstract

We discover that *hcp* phases of Fe and $Fe_{0.9}Ni_{0.1}$ undergo an electronic topological transition at pressures of about 40 GPa. This topological change of the Fermi surface manifests itself through anomalous behavior of the Debye sound velocity, *c/a* lattice parameter ratio and Mössbauer center shift observed in our experiments. First-principles simulations within the dynamic mean field approach demonstrate that the transition is induced by many-electron effects. It is absent in one-electron calculations and represents a clear signature of correlation effects in *hcp* Fe.

Iron is the most abundant element on our planet. It is one of the most important technological materials and, at the same time, one of the most challenging elements for the modern theory. As a consequence, the study of iron and iron-based alloys has been a focus of experimental and computational research over the past decades. Recently, investigations of phase relations and physical properties of iron and its alloys at high pressure led to new exciting discoveries including evidence for a body-centred-cubic (bcc) phase of iron-nickel alloy at conditions of the Earth's core [1] and the observation of superconductivity in the high-pressure hexagonal close packed (*hcp*) phase of iron in the pressure range 15-30 GPa and at temperatures below 2 K [2].

While the structural properties of iron and iron-nickel alloys at pressures below 100 GPa are well established [3], their electronic and magnetic properties are still debated. The α-phases (*bcc*) of Fe and $Fe_{0.9}Ni_{0.1}$ are ferromagnetic at ambient conditions, but an accurate description of the electronic structure of α-Fe and its high-temperature magnetism require a proper treatment of the many-electron effects [4]. The γ-phases (face-centered cubic, *fcc*) are believed to have complex incommensurate magnetic ground states, which are still not reproduced by theory [5]. The importance of correlation effects for the description of the α- to γ-phase transition in Fe at elevated temperature and ambient pressure has been recently underlined [6]. The ε-phases (*hcp*) of Fe and $Fe_{0.9}Ni_{0.1}$ were previously believed to be nonmagnetic [7]; however recent theoretical work showed that a collinear antiferromagnetic state (AFM-II) [8–10] or a more complex

67 AFM state [11] have lower energy than the nonmagnetic state. Nevertheless, the AFM-II

68 phase could not be resolved in Mössbauer experiments. Moreover, theoretical estimates

69 of the Néel temperature T_N yield a maximum value of ~69 K for *hcp* Fe at the transition

70 pressure (12 GPa), followed by a decrease with increasing pressure [12]. Although nickel

71 atoms are predicted to enhance the magnetic moments on neighboring iron atoms, there is

72 no evidence that ε-$Fe_{0.9}Ni_{0.1}$ is a static antiferromagnet down to at least 11 K at

73 21 GPa [10], implying that direct comparison is unreliable between static (0 K) *ab initio*

74 calculations for AFM ε-Fe and room temperature experimental data that clearly indicate a

75 paramagnetic phase. It is worth noting that *hcp* Fe becomes superconducting in the same

76 pressure range [2], and that the mechanism of superconductivity is believed to be

77 unconventional [13]. These observations indicate that the physical behavior of *hcp* Fe at

78 moderate pressures below 70 GPa is complex and the role of correlation effects beyond

79 the standard density-functional (DFT) approach in the physics of this material is not well

80 understood.

81   In order to unravel the evolution of the electronic structure in *hcp* Fe and $Fe_{0.9}Ni_{0.1}$

82 under pressure we have carried out a combined experimental and theoretical

83 investigation. We have extracted the Debye sound velocity V_D for pure Fe and $Fe_{0.9}Ni_{0.1}$

84 alloy from nuclear inelastic scattering (NIS) experiments as well as precisely measured

85 the lattice parameter *c/a* ratio and the Mössbauer centre shift in the pressure range from

86 12 to 70 GPa. All of our results show anomalous behavior at a similar pressure ~ 40 GPa.

87 Our state-of–the-art *ab initio* simulations within the dynamical mean-field theory [14–16]

88 reveal an electronic topological transition (ETT) in the *hcp* phase of iron at pressures of

89 about 30-40 GPa, providing an explanation of the experimentally observed anomalies.

90 The absence of the ETT in conventional one-electron DFT calculations demonstrates that

91 many-body correlation effects determine the Fermi surface topology of paramagnetic *hcp*

92 Fe, and, therefore, essential for the correct description of the complex physical

93 phenomena observed in this material.

94   Figure 1 summarizes our experimental measurements of the Debye sound velocity V_D

95 for Fe and $Fe_{0.9}Ni_{0.1}$ extracted from NIS experiments (technical details are given in

96 Supplementary Information [17]). The experimental data show a softening of V_D in the

97 pressure range 42-52 GPa. To verify our results we also analyzed the available

98   literature [18–21] and conclude that the same softening of V_D has been observed at
99   pressures of 40-50 GPa. The phenomenon was not given much attention in the previous
100   publications, perhaps due to data scatter and the uncertainties of individual data points.

101   The softening of the Debye sound velocity in Fig. 1 is weak, so we made further
102   investigations. We measured the lattice parameters of *hcp*-Fe in a diamond anvil cell
103   (DAC) on compression to ~65 GPa in quasi-hydrostatic He pressure transmitting medium
104   at ambient temperature and found an anomaly in *c/a* at about 40 GPa (Fig. 2a), consistent
105   with the pressure at which V_D shows softening. The pressure dependence of the *c/a* ratio
106   in *hcp* Fe has been the subject of several previous experimental studies [22–27] that were
107   mainly focused on much higher pressures. However, a closer inspection of the results by
108   Dewaele *et al.* [24] shows very good agreement with our data (*Fig. S.1.3* [17]). Also, an
109   anomalous behavior of *c/a* was reported at about 50 GPa based on a limited number of
110   data points collected in DAC experiments using a non-hydrostatic (NaCl) pressure-
111   transmitting medium [27].

112   Mössbauer spectroscopy can also be a powerful method to detect pressure-induced
113   transitions [28]. We performed Mössbauer experiments on pure Fe and $Fe_{0.9}Ni_{0.1}$ up to
114   60 GPa in a DAC loaded with He as a quasi-hydrostatic pressure transmitting medium,
115   and observed a large anomaly in the center shift variation with pressure at 40-45 GPa
116   (Fig. 2b). Our theoretical calculations demonstrate that the anomaly cannot be explained
117   by changes of the electron density at the nuclei and, correspondingly, of the isomer
118   shift [17]. Therefore, the anomaly must be associated with the second-order Doppler
119   shift [28].

120   We have shown from three independent experimental methods pressure-induced
121   anomalies in the pressure range 40-50 GPa. We note that X-ray diffraction does not
122   reveal any crystallographic structural change of *hcp*-Fe and $Fe_{0.9}Ni_{0.1}$ at the same
123   conditions [1,29,30], and as discussed above, there is no long range magnetic order in the
124   *hcp* phase of Fe detected by experiments. The observed anomalies must therefore be
125   associated with changes in the electronic state of paramagnetic *hcp*-Fe and $Fe_{0.9}Ni_{0.1}$. To
126   address this question we made a theoretical investigation of the electronic structure of ε-
127   Fe at moderate pressures in the range 12-70 GPa. We employed a state-of-the-art fully
128   self-consistent technique [16] combining full-potential linearized augmented plain-wave

129 (LAPW) band structure method with the dynamical mean-field theory (DMFT) treatment

130 of the on-site Coulomb repulsion between Fe $3d$ states [17]. The DMFT quantum

131 impurity problem was solved using the exact Continuous-time strong-coupling Quantum

132 Monte-Carlo method [31]. A combination of LDA and DMFT has been applied

133 previously to investigate thermodynamic stability [6] and to describe the magnetic

134 properties [4] of paramagnetic bcc Fe at ambient pressure, which justifies the choice of

135 method for this work.

136 The LDA+DMFT Fermi surfaces and $\boldsymbol{k}$-resolved spectral functions for two different

137 volumes are shown in Fig. 3. The hcp phase of Fe is predicted to be weakly correlated,

138 with the average mass enhancement decreasing from 1.43 at 16 GPa to 1.25 at 69 GPa,

139 indicating a reduced correlation strength at smaller volumes. Sharp bands in the vicinity

140 of the Fermi level ε_F and a noticeable shift of bands toward ε_F compared to the LDA

141 picture (Fig. 3 (e) and (f)) are the usual features of a Fermi liquid. Most interestingly, the

142 hole-like bands at the Γ and $\mathbf{L}$ points visible at smaller volume are found $below$ ε_F at

143 V=10.4 Å^3/at. Hence, the DMFT calculations show that the topology of the Fermi surface

144 changes under compression. Indeed a comparison of Figs. 3 (a) and (b) shows that hole

145 pockets appears at Γ and $\mathbf{L}$ with decreasing volume, and therefore hcp Fe undergoes an

146 $electronic$ $topological$ $transition$ [32] under applied pressure. The actual ETT takes place

147 at P~30 GPa. It is remarkable that the observed ETT is absent in the LDA calculations; it

148 appears only upon inclusion of correlation effects.

149 The effects of ETT on the lattice properties of metals within the one-electron

150 approximation are well understood [33]. The elastic moduli C_{ii} calculated at the

151 condition of constant particle number at the deformation contains the contribution

$$\delta C_{ii} = -\frac{1}{V_0} \sum_{\lambda} \left(\frac{\partial \xi_{\lambda}}{\partial u_i} \right)^2 \delta(\xi_{\lambda}), \qquad (1)$$

153 where $\xi_{\lambda} = \varepsilon_{\lambda} - \varepsilon_F$, and ε_{λ} denotes the single-particle energies. ξ_{λ} is singular near the

154 ETT, and this singular contribution has the same singularity as $-N(\varepsilon_F)$. This means, in

155 particular, that the peculiarity in the Debye sound velocity is $\varDelta V_D \sim -\delta N(E_F)$, where $\delta N(E_F)$

156 is the change in the density of states (DOS) at the Fermi level due to ETT. In the case of

157 an appearance of a new hole pocket below the critical volume V_{ETT} the change in DOS is

158 $\delta N(E_F) \sim (V_{ETT}-V)^{1/2}$, hence the one-electron theory predicts the existence of square-root-

159 down-shaped peculiarity at the ETT. Our DMFT calculations show that in the case of

160 *hcp*-Fe at moderate compression one should use the Fermi-liquid theory of ETT [34]. In

161 this case many-electron effects cause the singularity of the thermodynamic potential Ω at

162 ETT to be two-sided. Still the leading term is a square root in ΔV_D on one side of the

163 transition, while the peculiarity on the other side of the transition is one power weaker.

164   The Debye temperature θ_D also has a singularity as $-N(\varepsilon_F)$, and lattice heat capacity

165 at low temperature $T \ll \theta_D$ has the same singularity as the electron heat capacity. The

166 thermal expansion coefficient proportional to the derivative of θ_D with respect to

167 deformation has a stronger singularity at these temperatures, like $\dfrac{\partial N(\varepsilon_F)}{\partial \varepsilon_F}$, that is

168 divergent at the point of ETT (e.g.,   [35]). It is important to stress, however, that the

169 Debye model is qualitatively incorrect in the situation of ETT. Strong anomalies of the

170 phonon spectra in the harmonic approximation occur in a relatively small part of the

171 Brillouin zone near the Γ point and the average phonon frequency over the whole

172 Brillouin zone, which is relevant for thermodynamics at $T \approx \theta_D$, is weaker by a factor of

173 $\varepsilon_F - \varepsilon_c$, where ε_c is the Van Hove singularity energy [36]. However, if we take into

174 account quasiharmonic and anharmonic effects, i.e., the temperature dependence of

175 phonon frequencies due to thermal expansion and phonon-phonon interactions, the

176 singularities again enhance and become like $N(\varepsilon_F)$ in average phonon frequencies and

177 like $\dfrac{\partial N(\varepsilon_F)}{\partial \varepsilon_F}$ in the elastic moduli [36].

178   For *hcp* metals ETTs have been associated with anomalies in the lattice parameter

179 ratio *c/a* in the vicinity of the transition [37–40]. The dependence of lattice constants on

180 the external parameters is less singular than C_{ii} since they are related to the first

181 derivatives of the thermodynamic potential, while C_{ii} are related to the second

182 derivatives. This means that the anomaly in the *c/a* ratio at zero temperature should be

183 hardly visible but at finite (and sufficiently high) temperatures it is proportional to $N(\varepsilon_F)$

184 via the anomaly of the thermal expansion coefficient, discussed above. The same is true

185 for the second-order Doppler shifts of the Mössbauer spectra related to the heat capacity

186   and, thus, with the average phonon frequencies over the Brillouin zone. Thus, the theory

187   of ETT provides a convincing explanation of the experimentally observed anomalies of

188   the sound velocity, *c/a* ratio and center shift at 40-45 GPa.

189   To conclude, we observe the electronic isostructural transition of *hcp* Fe and $Fe_{0.9}Ni_{0.1}$

190   at a pressure of ~40 GPa. The presence of the transition is confirmed by three

191   independent experimental approaches – nuclear inelastic scattering, *c/a* ratio

192   measurement, and Mössbauer center shift determination. The theoretical calculations

193   carried out by means of state-of-the-art *ab initio* methods explain the anomalies in terms

194   of a change of the Fermi surface topology, a so-called electronic topological transition.

195   The existence of the ETT in many-body calculations and its absence in one-electron

196   calculations is a clear signature of correlation effects in the paramagnetic phase of *hcp*

197   Fe. Therefore, advanced approaches beyond the density functional theory are needed to

198   understand the complex physics of this material. Our results also point out to possible

199   importance of many-body effects in other itinerant metallic systems at high-pressure

200   conditions.

209

210   REFERENCES

211   [1]   L. Dubrovinsky, N. Dubrovinskaia, O. Narygina, I. Kantor, A. Kuznetzov, V. B.

212   Prakapenka, L. Vitos, B. Johansson, A. S. Mikhaylushkin, S. I. Simak, and I. A.

213   Abrikosov, Science **316**, 1880 (2007).

214   [2]   K. Shimizu, T. Kimura, S. Furomoto, K. Takeda, K. Kontani, Y. Onuki, and K.

215   Amaya, Nature **412**, 316 (2001).

216   [3]   R. Boehler, Rev. Geophys. **38**, 221 (2000).

217 [4]   A. I. Lichtenstein, M. I. Katsnelson, and G. Kotliar, Phys. Rev. Lett. **87**, 067205

218 (2001).

219 [5]   I. A. Abrikosov, A. E. Kissavos, F. Liot, B. Alling, S. I. Simak, O. Peil, and A.

220 V. Ruban, Phys. Rev. B **76**, 014434 (2007).

221 [6]   I. Leonov, A. Poteryaev, V. Anisimov, and D. Vollhardt, Phys. Rev. Lett. **106**,

222 106405 (2011).

223 [7]   G. Cort, R. D. Taylor, and J. O. Willis, J. Appl. Phys. **53**, 2064 (1982).

224 [8]   G. Steinle-Neumann, L. Stixrude, and R. E. Cohen, Phys. Rev. B **60**, 791 (1999).

225 [9]   G. Steinle-Neumann, R. E. Cohen, and L. Stixrude, J. Phys.: Condens. Matter **16**,

226 S1109 (2004).

227 [10]   A. B. Papandrew, M. S. Lucas, R. Stevens, I. Halevy, B. Fultz, M. Y. Hu, P.

228 Chow, R. E. Cohen, and M. Somayazulu, Phys. Rev. Lett. **97**, 087202 (2006).

229 [11]   R. Lizárraga, L. Nordström, O. Eriksson, and J. Wills, Phys. Rev. B **78**, 064410

230 (2008).

231 [12]   V. Thakor, J. B. Staunton, J. Poulter, S. Ostanin, B. Ginatempo, and E. Bruno,

232 Phys. Rev. B **67**, 180405 (2003).

233 [13]   I. I. Mazin, D. A. Papaconstantopoulos, and M. J. Mehl, Phys. Rev. B **65**, 100511

234 (2002).

235 [14]   A. Georges, G. Kotliar, W. Krauth, and M. J. Rozenberg, Rev. Mod. Phys. **68**, 13

236 (1996).

237 [15]   G. Kotliar, S. Y. Savrasov, K. Haule, V. S. Oudovenko, O. Parcollet, and C. A.

238 Marianetti, Rev. Mod. Phys. **78**, 865 (2006).

239 [16]   M. Aichhorn, L. Pourovskii, V. Vildosola, M. Ferrero, O. Parcollet, T. Miyake,

240 A. Georges, and S. Biermann, Phys. Rev. B **80**, 085101 (2009).

241 [17]   see Supplementary information at [URL] for details of experiments and

242 theoretical simulations.

243 [18]   H. K. Mao, J. Xu, V. V. Struzhkin, J. Shu, R. J. Hemley, W. Sturhahn, M. Y. Hu,

244 E. E. Alp, L. Vocadlo, D. Alfè, G. D. Price, M. J. Gillan, M. Schwoerer-Böhning, D.

245 Häusermann, P. Eng, G. Shen, H. Giefers, R. Lübbers, and G. Wortmann, Science **292**,

246 914 (2001).

247 [19]   R. Lübbers, H. F. Grünsteudel, A. I. Chumakov, and G. Wortmann, Science **287**,

248   1250 (2000).

249   [20]   J. C. Crowhurst, A. F. Goncharov, and J. M. Zaug, in *Advances in High-Pressure*

250   *Technology for Geophysical Applications* (Elsevier, 2005), pp. 3–23.

251   [21]   J. F. Lin, V. V. Struzhkin, W. Sturhahn, E. Huang, J. Zhao, Y. M. Hu, E. E. Alp,

252   H.-K. Mao, N. Boctor, and R. J. Hemley, Geophys. Res. Lett. **30**, (2003).

253   [22]   H.-K. Mao, Y. Wu, L. C. Chen, J. F. Shu, and A. P. Jephcoat, J. Geophys. Res.

254   **95**, 21737 (1990).

255   [23]   L. S. Dubrovinsky, S. K. Saxena, F. Tutti, S. Rekhi, and T. LeBehan, Phys. Rev.

256   Lett. **84**, 1720 (2000).

257   [24]   A. Dewaele, P. Loubeyre, F. Occelli, M. Mezouar, P. I. Dorogokupets, and M.

258   Torrent, Phys. Rev. Lett. **97**, 215504 (2006).

259   [25]   Y. Ma, M. Somayazulu, G. Shen, H. Mao, J. Shu, and R. J. Hemley, Physics of

260   the Earth and Planetary Interiors **143–144**, 455 (2004).

261   [26]   R. Boehler, D. Santamaría-Pérez, D. Errandonea, and M. Mezouar, Journal of

262   Physics: Conference Series **121**, 022018 (2008).

263   [27]   S. Ono, T. Kikegawa, N. Hirao, and K. Mibe, American Mineralogist **95**, 880

264   (2010).

265   [28]   W. Potzel, M. Steiner, H. Karzel, W. Schiessl, M. Köfferlein, G. M. Kalvius, and

266   P. Blaha, Phys. Rev. Lett. **74**, 1139 (1995).

267   [29]   C. S. Yoo, J. Akella, A. J. Campbell, H. K. Mao, and R. J. Hemley, Science **270**,

268   1473 (1995).

269   [30]   W. L. Mao, A. J. Campbell, D. L. Heinz, and G. Shen, Physics of the Earth and

270   Planetary Interiors **155**, 146 (2006).

271   [31]   P. Werner, A. Comanac, L. de' Medici, M. Troyer, and A. Millis, Phys. Rev.

272   Lett. **97**, 076405 (2006).

273   [32]   I. M. Lifshitz, Soviet Phys. JETP **11**, 1130 (1960).

274   [33]   M. I. Katsnelson, I. I. Naumov, and A. V. Trefilov, Gpht **49**, 143 (1994).

275   [34]   M. I. Katsnelson and A. V. Trefilov, Phys. Rev. B **61**, 1643 (2000).

276   [35]   P. Souvatzis, O. Eriksson, and M. I. Katsnelson, Phys. Rev. Lett. **99**, 015901

277   (2007).

278   [36]   V. G. Vaks and A. V. Trefilov, J. Phys.: Condens. Matter **3**, 1389 (1991).

279   [37]   S. Meenakshi, V. Vijayakumar, B. K. Godwal, and S. K. Sikka, Phys. Rev. B **46**,

280   14359 (1992).

281   [38]   D. L. Novikov, A. J. Freeman, N. E. Christensen, A. Svane, and C. O. Rodriguez,

282   Phys. Rev. B **56**, 7206 (1997).

283   [39]   V. V. Kechin, Phys. Rev. B **63**, 045119 (2001).

284   [40]   Z. Li and J. S. Tse, Phys. Rev. Lett. **85**, 5130 (2000).

285

Figure captions:

287 **Figure 1 (color online)**

288 Debye sound velocity V_D as a function of pressure for pure iron (filled black squares, -1-)

289 and $Fe_{0.9}Ni_{0.1}$ alloy (open triangles,-2-).. The upper axis shows the density scale. Also

290 shown are literature data on sound velocities obtained with NIS (open circles [18],-4- and

291 half-filled circles [19],-5-), and impulsive stimulated light scattering (ISLS)

292 measurements [20] (circles with crosses, -6-) for pure ε-Fe, as well as NIS data [21] for

293 ε-$Fe_{0.92}Ni_{0.08}$ (blue open squares,-3-). Experimental data presented in the figure show the

294 softening of V_D in a pressure region of 42-52 GPa.

295

296 **Figure 2**

297 Experimental pressure dependence of (a) *hcp* phase lattice parameter c/a ratio and (b) the

298 Mössbauer centre shift based on several experimental datasets for pure iron (red circles)

299 and for $Fe_{0.9}Ni_{0.1}$ alloy (blue circles). The centre shift values are given relative to pure *bcc*

300 iron. Straight grey lines in (a) are guides for the eye.

301

302 **Figure 3.**

303 The LDA+DMFT k-resolved spectral function $A(k,E)$ (in V_{at}/eV, where V_{at} is the volume

304 per atom) of *hcp* Fe at volumes of 8.9 $Å^3$/at (*a*) and 10.4 $Å^3$/at (*b*) corresponding to

305 pressures of 69 and 15.4 GPa, respectively. The energy zero is taken at the Fermi level.

306 The hole-like bands at the **Γ** and **L** points at volume 8.9 $Å^3$/at (indicated by the white

307 arrows) are *below* E_F at V=10.4 $Å^3$/at. The corresponding LDA band structures are shown

308 in *e* and *d*, respectively. In (e) and (f) the corresponding LDA+DMFT Fermi surfaces are

309 shown for the same volumes. The full Fermi surface is plotted on the left-hand side and

310 its cut along the Γ-M direction is displayed in the right-hand side. Changes of the FS

311 topology around the L and Γ points are clearly seen.
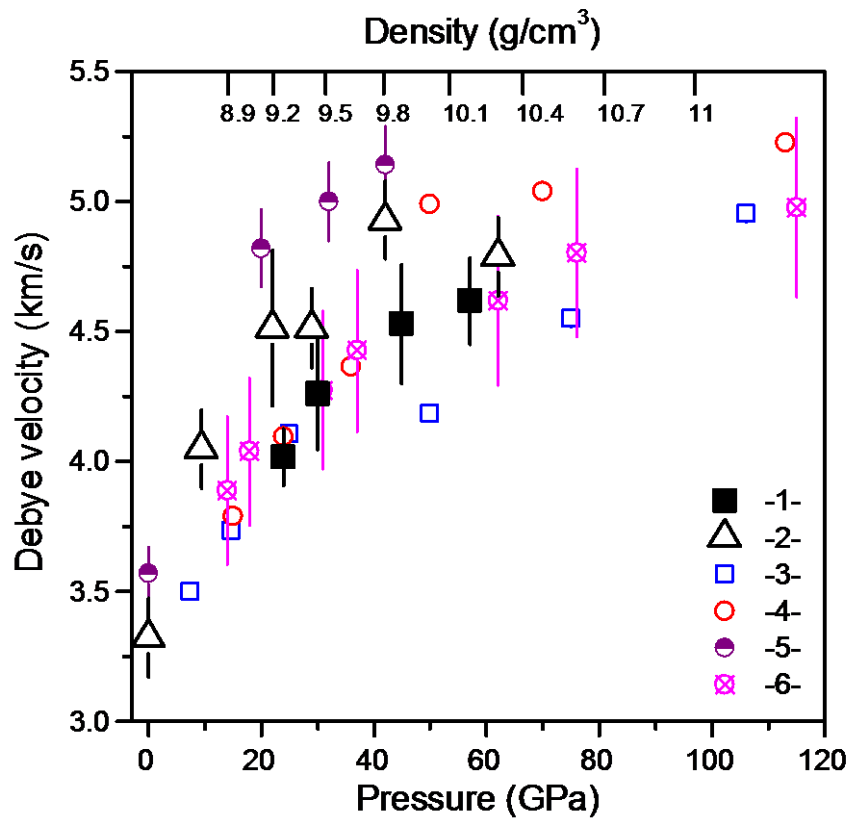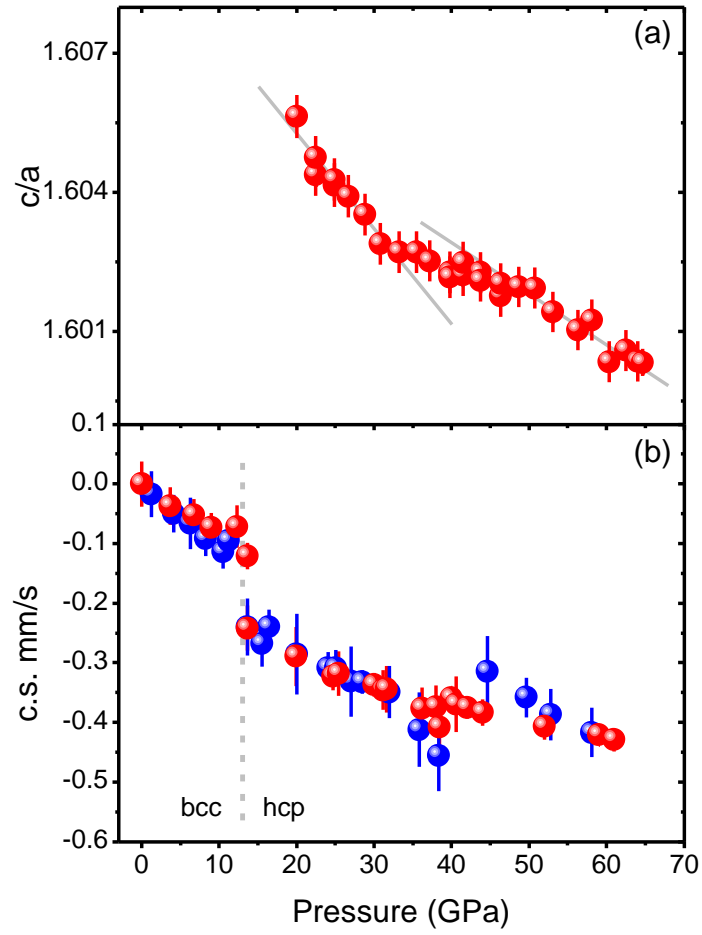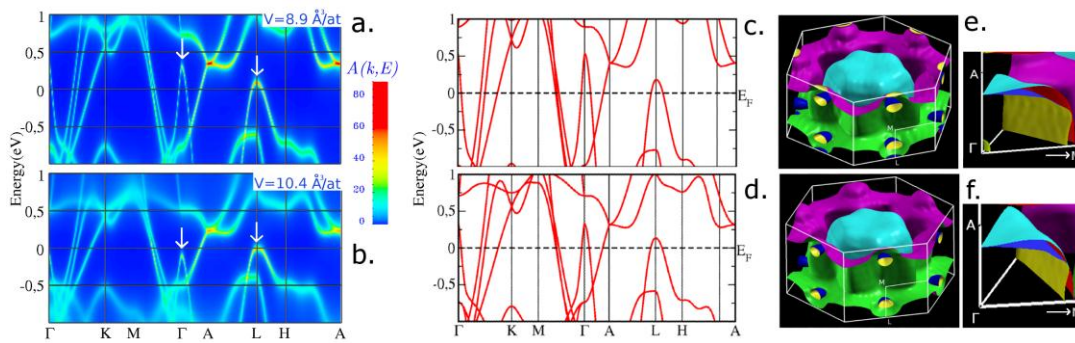
312

313

FIG. 1 (color online)

314

FIG. 2

FIG. 3.

315

316

SUPPLEMENTARY INFORMATION

318   *1.   Experimental details*

319

320   For the preparation of the iron sample we used enriched [57]Fe of 99.99% purity. The

321 $Fe_{0.9}Ni_{0.1}$ samples were prepared by mixing appropriate amounts of [57]Fe enriched iron

322 and nickel powder of 99.999% purity. The mixture was compressed to 2 GPa in a piston-

323 cylinder apparatus, heated above the melting point and subsequently quenched.

324   To achieve high pressures in different experiments we used two types of diamond

325 anvil cells: one piston-cylinder conventional cell for Mossbauer experiments, with He gas

326 for quasi-hydrostatic conditions loaded into a chamber of Re gasket, and for nuclear

327 inelastic x-ray scattering (NIS) another panoramic cell produced in Bayerisches

328 Geoinstitut. Special types of new cells slits make it possible to measure nuclear forward

329 scattering (NFS) or X-Ray diffraction patterns at the same time as NIS, and, due to the

330 specific geometry of NIS cells, Be was chosen as a material for the gaskets. We used LiF

331 as a pressure medium for the NIS cells. In both experiments we used diamonds with

332 250μm culet size and small ruby chips to measure the pressure inside gasket chambers.

333 The prepared gasket chambers were 60μm·20μm and 100μm·30μm (diameter·height) for

334 NIS and Mossbauer experiments, respectively.

335   NIS studies were carried out at the beam line ID18 [S1] (ESRF, Grenoble); the

336 details of the experiment are described in Lübbers et al. [S2] and references therein. Data

337 analysis was performed using program DOS-2.1 according to the calculation procedure

338 described in Kohn and Chumakov [S3], and more details of the calculation procedure is

339 described in Sturhahn [S4] and references therein.

340   To extract the partial density of states for iron (PDOS) using NIS we employed the

341 following procedure. First, we collected absorption spectra of the sample enriched with

342 [57]Fe as a function of the energy of incident radiation (NIS spectra Fig S1.1). After

343 extracting the elastic contribution to the NIS spectra, we used DOS-2.1 software to

344 extract the PDOS. Next, we calculated Debye sound velocities (V_D) using the

345 relation [S5]:

346 $$\rho \cdot V_D{}^3 = \frac{4 \cdot \pi \cdot \tilde{m}}{h^3} \cdot \lim_{E \to 0} \frac{E^2}{D(E)},$$

347   where ρ is the density of the material; $\tilde{m}$ is the mass of the nuclear resonant isotope

348   (^{57}Fe); h is Planck's constant; $D(E)$ is the iron PDOS and E is energy.

349   We determined the equation of state for the *hcp* phase of Fe and $Fe_{0.9}Ni_{0.1}$ (the

350   variation of ρ with pressure) and the bulk modulus in a separate synchrotron X-ray

351   diffraction experiment on beam lines ID09a (ESRF, Grenoble) and IDD-13 (APS,

352   Argonne). The parameters derived from a fit to the Birch-Murnaghan equation of state for

353   *hcp*-$Fe_{0.9}Ni_{0.1}$ are bulk modulus K=159(3) GPa, K'=4.78(9) and V_0=6.77(1) cm^3/mol, and

354   for *hcp*-Fe EOS these parameters have values indistinguishable from the values reported

355   in previous studies [S6,S7]. We collected a set of X-ray diffraction data for pure Fe in a

356   compression run up to ~65 GPa (quasi-hydrostatic pressure medium - He). We used the

357   ruby fluorescence method for pressure determination [S8] and Fullprof [S9] and

358   Unitcell [S10] programs to extract the c and a lattice parameters for *hcp*-Fe. There is a

359   remarkable agreement between values calculated by these programs. A representative X-

360   diffraction pattern from the second run is shown in Fig. S1.2. The results of our runs are

361   compared in Fig. S1.3 with data from the literature [S11,S12].

362   ^{57}Fe Mössbauer spectra (MS, Fig S1.4) were recorded at room temperature in

363   transmission mode on a constant acceleration Mössbauer spectrometer using a nominal

364   370 MBq ^{57}Co high specific activity source in a 12 μm Rh matrix (point source). The

365   velocity scale was calibrated relative to 25 μm α-Fe foil. Mössbauer spectra were fitted to

366   Lorentzian lineshapes using the commercially available fitting program NORMOS

367   written by R.A. Brand (distributed by Wissenschaftliche Elektronik GmbH, Germany).

368   Collection time for each spectrum varied from 24 to 48 h.

369   In our experiments the *bcc* α-phase transforms to the *hcp* ε-phase at 10-13 GPa, in

370   good agreement with literature data [S13,S14]. The center shift in hcp-Fe and hcp-

371     $Fe_{0.9}Ni_{0.1}$ gradually decreases with pressure, up to 40-45 GPa. In this pressure range we

372   observe an abrupt increase of the center shift by ~0.15 mm/s in $Fe_{0.9}Ni_{0.1}$ and a smaller

373   value of ~0.05 mm/s in pure iron (Fig. 2, main text). Upon further compression to 60 GPa

374   we see no sign of further irregular behavior. The discontinuity was observed in several

375   independent DAC loadings. Previous X-ray diffraction measurements have not revealed

376   any structural transformation in the pressure range 13-60 GPa in both *hcp* Fe and

377     $Fe_{0.9}Ni_{0.1}$ [S15,S16].
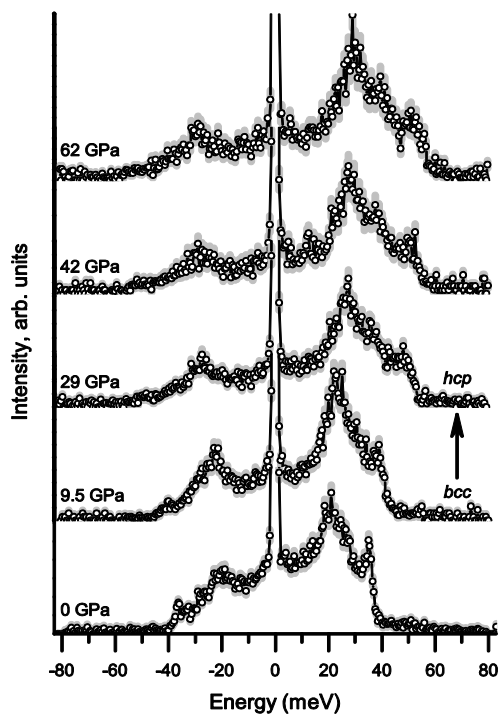
Fig. S1.1 Nuclear inelastic scattering absorption spectra at various pressures measured on $Fe_{0.9}Ni_{0.1}$.

378
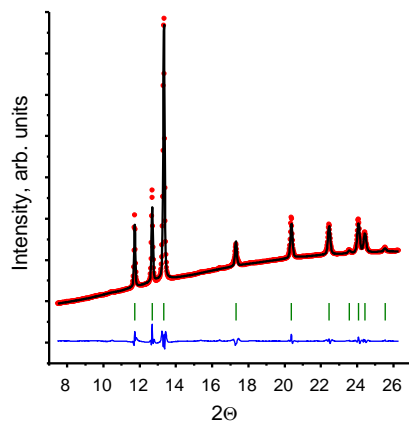
Fig. S1.2 X-ray diffraction pattern of pure Fe obtained at 64.7(1) GPa. The red data points are the experimental data. The black line, the blue line and the green vertical lines represent a Le Bail fit of data (Fullprof), difference between the data and the model, and positions of *hcp*-Fe diffraction lines, respectively.
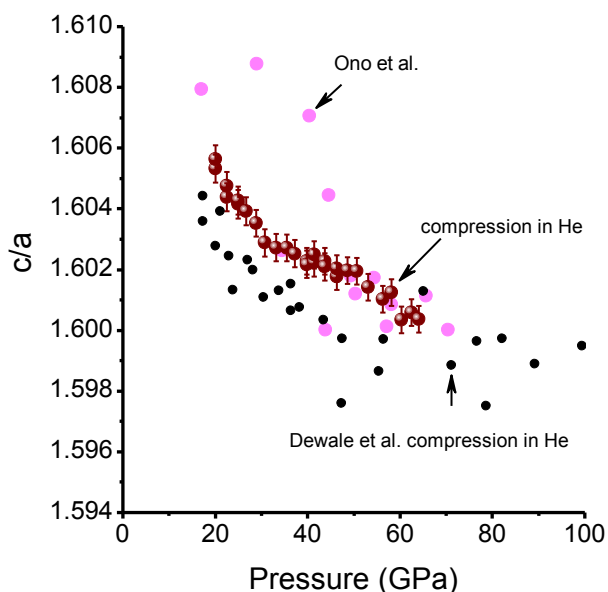
Fig S1.3 Variation of *c/a* lattice parameter ratio as a function of pressure. Dark red points correspond to our data (He pressure medium), and pink points indicate those obtained by Ono et al. [S11] (NaCl pressure medium, experimental uncertainties unknown) collected during compression runs. The Dewaele *et al*. [S12] data are shown by black closed circles.

379

380
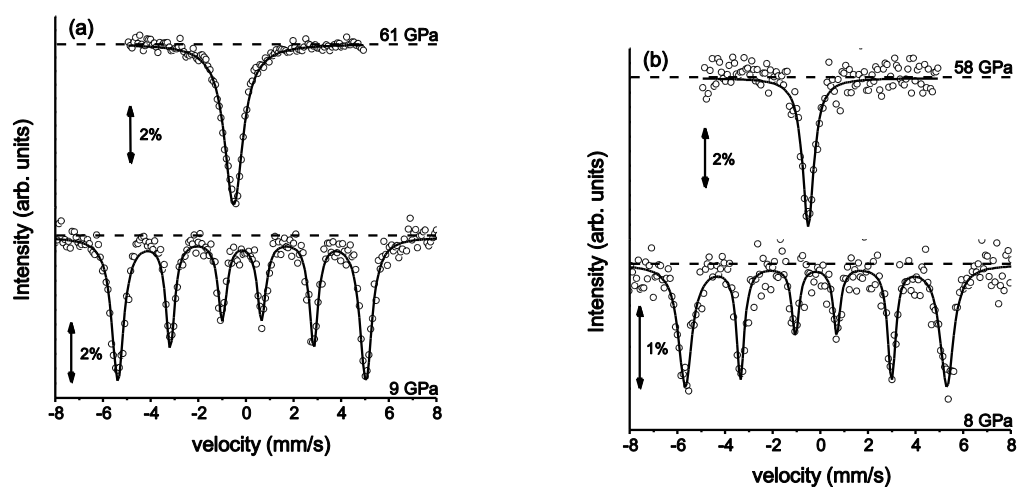
Fig. S1.4 Representative Mössbauer spectra of (a) pure Fe and (b) $Fe_{0.9}Ni_{0.1}$ samples at the indicated pressures. Solid lines represent model fits.

381   *2 Theoretical Simulations*

382   *2.1 Local-density approximation+dynamical mean-field theory (LDA+DMFT)*
383   *approach*

384   Our LDA+DMFT calculations have been performed with a full-potential fully-self

385   consistent implementation [S17,S18] combining the dynamical-mean-field-theory [S19–

386   S21] and a highly precise full-potential linearized augmented plane wave (FLAPW)

387   electronic structure technique [S22]. The DMFT quantum impurity problem was solved

388   by the continuous-time quantum Monte Carlo (CTQMC) [S23] method. At the beginning

389   of each LDA+DMFT iteration, the eigenvalues and eigenvectors of the Kohn-Sham

390   problem were obtained by the FLAPW code. Wannier-like functions for the Fe-3d shell

391   were then constructed by projecting local orbitals onto a set of FLAPW Bloch states

392   located within the energy window from -9.5 to 9.2 eV (details of the projection procedure

393   can be found elsewhere [S17]). We then introduced a local Coulomb interaction acting

394   between those Wannier orbitals and solved the resulting many-body problem within the

395   DMFT framework. After completing the DMFT cycle we calculated the resulting density

396   matrix in the Bloch states' basis, which was then used to recalculate the charge density

397   and update the Kohn-Sham potential at the next iteration [S18].

398   We have employed the density-density form of the local Coulomb interaction in the

399   spherical approximation, in which case the interaction matrix is fully specified by the

400   parameters U=3.4 eV and J=0.9 eV, these values of U (or Slater parameter F_0) and J

401   were obtained in recent constrained random-phase approximation calculations for *bcc*

402   Fe [S24] (note that the parameter U reported in Ref. 22 is the on-site repulsion $U_{mm}^{\uparrow\downarrow}$

403   between electrons of opposite spins located on the same orbital as well as

404    $J = \dfrac{1}{N(N-1)} \sum\limits_{m \neq m'}^{N} \left(U_{mm'}^{\uparrow\downarrow} - U_{mm'}^{\uparrow\uparrow} \right)$, which, after conversion in accordance with formulae

405   provided in Ref. 15, gives the values used in the present work). The quantum impurity

406   problem has been solved with 3 million CTQMC cycles with each cycle consisting of 200

407   CTQMC moves following by a measurement. The *hcp* phase under consideration is a

408 metal with a rather uniform occupancy of the orbitals within the Fe $3d$ shell. Therefore,

409 we employed the around mean-field form [S25] for the double-counting correction term.

410 The CTQMC solver computes the Green's function on the imaginary-time axis so an

411 analytic continuation is needed in order to obtain results on the real axis. For that we use

412 a stochastic version of the Maximum Entropy method [S26] with which we calculate the

413 retarded lattice Green's function, $G_{\nu\nu}(k,\omega^+)$, where ν labels all the Bloch bands

414 considered. We finally obtain the spectral function as

415

416

417 follows:

418 $$A(k,\omega) = -\frac{1}{\pi}\mathrm{Im}\left[\sum_{\nu}G_{\nu\nu}(k,\omega^+)\right].$$

419

420 *2.2 Isomer shift calculations in Fe*
421

422 The Mössbauer centre shift of the absorption line, ΔE^C, is composed of two

423 contributions:

424 $$\Delta E^C = \delta^{IS} + \delta^{SOD},$$

425 called the isomer shift (IS) and the second-order Doppler shift (SOD), respectively. The

426 latter is a relativistic Doppler shift of the photon frequency due to the relative velocity, v

427 , of the source and absorber. Due to the thermal motion of the ions, the corresponding

428 shift of the absorption line E_γ depends on v to second order as:

429 $$\delta^{SOD} = \frac{\langle v^2 \rangle}{2c^2}E_\gamma,$$

430 where c is the speed of light. The isomer shift, which is due to the different chemical

431 environments of the source and the absorber, can in turn be calculated as:

432 $$\delta^{IS} = -\alpha[\rho_a(0) - \rho_s(0)],$$

433 where $\rho_a(0)$ and $\rho_s(0)$ are the electron densities in the absorber and the source

434 materials, respectively, evaluated at the nucleus. α is an empirical nuclear calibration

435 constant to which we assigned the value 0.27 a_0^3 mm/s, which is within the common

436 range reported in the literature [S27–S29]. We evaluated $\rho_a(0)$ and $\rho_s(0)$ from *ab initio*

437 calculations, based on the local density approximation (LDA) and local density

438 approximation + dynamical mean-field theory (LDA+DMFT) [S17–S21].

439 The pure LDA calculations were performed using two different computational

440 methods: exact muffin-tin orbitals (EMTOs) [S30] and FPLAPW [S22]. In EMTO

441 calculations, we treated 3d and 4d electron states as valence, and the core states were

442 recalculated in each iteration of the self-consistency cycle. The number of **k**-points in the

443 numerical integrals over the Brillouin zone was converged with respect to the total

444 energy to within 0.1 meV/atom. In FPLAPW calculations, electronic states were

445 separated into core- and valence-states at -6.0 Ry. The k-points were chosen from a mesh

446 of 10 000 points in the Brillouin zone, and we set the $R_{MT} * K_{\max}$ parameter to 8.0.

447 In DMFT+LDA calculations, the FPLAPW method was used for the LDA part, as

448 described in Sec. 2.1. We used the experimental lattice constants at the corresponding

449 pressures, which gives a highly accurate description of electronic structure at fixed

450 volume [S31]. The source system was taken to be body-centered cubic (*bcc*) Fe at

451 ambient pressure, in order to emulate the experimental set-up.

452 Since only *s*-orbitals have finite probability density at the origin, it is reasonable to

453 assume that δ^{IS} depends mainly on the difference in the *s*-electron charge density at the

454 absorber and emitter nuclei. In the electronic structure computational methods employed

455 in this work, the nucleus is assumed to be point-like and to be situated at the origin. As

456 the *s*-electron wave function diverges in this limit, we have modeled the nucleus as a

457 uniformly charged sphere of radius R_n, where:

458 $$R_n = CA^{1/3}$$

459 for an isotope of atomic mass *A*, and *C* = 1.25 fm [S32]. Rather than using the value

460 $\rho = \rho(r = R_n)$ in Eq. (3), we take the average density:

461 $$\langle\rho\rangle = \frac{4\pi}{V_n}\int_{R_0}^{R_n}\rho(r)r^2 dr$$

462 evaluated from the radial point R_0, which is chosen to lie very close to the origin.

463 We have performed calculations assuming a paramagnetic state. For the LSDA

464 calculations it was simulated by means of disordered local moments (DLM) [S33]. The

465   DLM state was treated using the coherent potential approximation (CPA) within the

466   EMTO framework [S30]. The magnitudes of the local moments were fixed to 0

467   (corresponding to non-magnetic calculations), 0.5, 1.0, and 1.5 μ_B in the entire volume

468   range. We also used values determined self-consistently as a function of volume using the

469   method developed in Ref. [S34], which includes longitudinal spin fluctuations in a

470   single-site mean-field approximation. Within the longitudinal spin fluctuation theory only

471   the so-called *on-site* longitudinal spin fluctuation energy, *E(m)*, is calculated by a

472   constrained DFT approach with electronic excitations at temperature *T*. Then, the average

473   value of the magnetic moment, *<m>,* is determined using the corresponding partition

474   function, Z_m, assuming that there is full coupling of the transverse and longitudinal

475   degrees of freedom:

476

$$\langle m \rangle = \frac{1}{Z_m} \int m^3 \exp(-E(m)/k_B T) dm$$

$$Z_m = \int m^2 \exp(-E(m)/k_B T) dm$$

477   the resulting average magnetic moments are shown in Fig. S2.2.1 as a function of volume

478   at 300 K.

479   Fig. S2.2.2 shows the calculated isomer shift as a function of unit cell volume in Fe,

480   which is also compared to experimental measurements of the center shift. Using LDA,

481   the trends of the obtained isomer shift follow the experimental center shift, and the shift

482   due to *bcc-hcp* transition is also seen. However, the anomaly observed in the

483   experimental center shift around the unit cell volume of 65 a.u.[3]/atom is not seen in the

484   calculated isomer shift, regardless of the assumed magnetic state.

485   Within the LDA+DMFT technique we obtain a slight offset with respect to the LDA

486   data. This offset is far greater than the statistical fluctuations of the isomer shift during

487   the computational iterations, which are indicated by error bars in Figure S2.2.2. The error

488   bars correspond to +/- 2 standard deviations of the obtained isomer shift during the final

489   ten iterations. In any case, the center shift anomaly is not seen in this case either.

490   Therefore, it should be attributed to the peculiarity of the second-order Doppler

491   shift [S35].
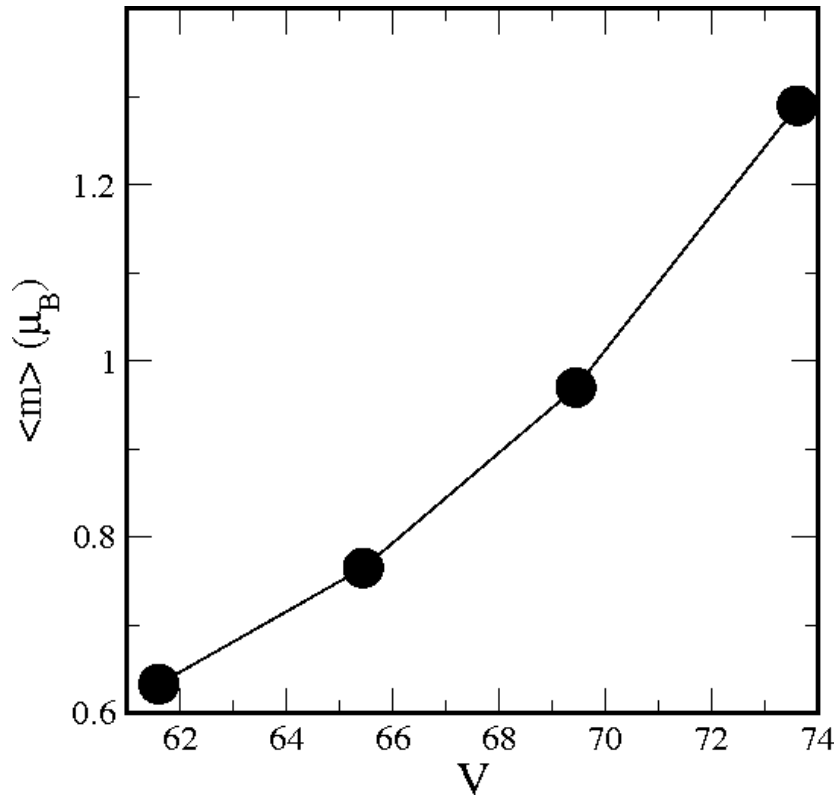
Fig. S2.2.1 Average magnetic moment in the paramagnetic state of hcp Fe at T=300K as a function of volume per atom (in Bohr^3), as calculated by means of the longitudinal spin fluctuation theory.

492
493
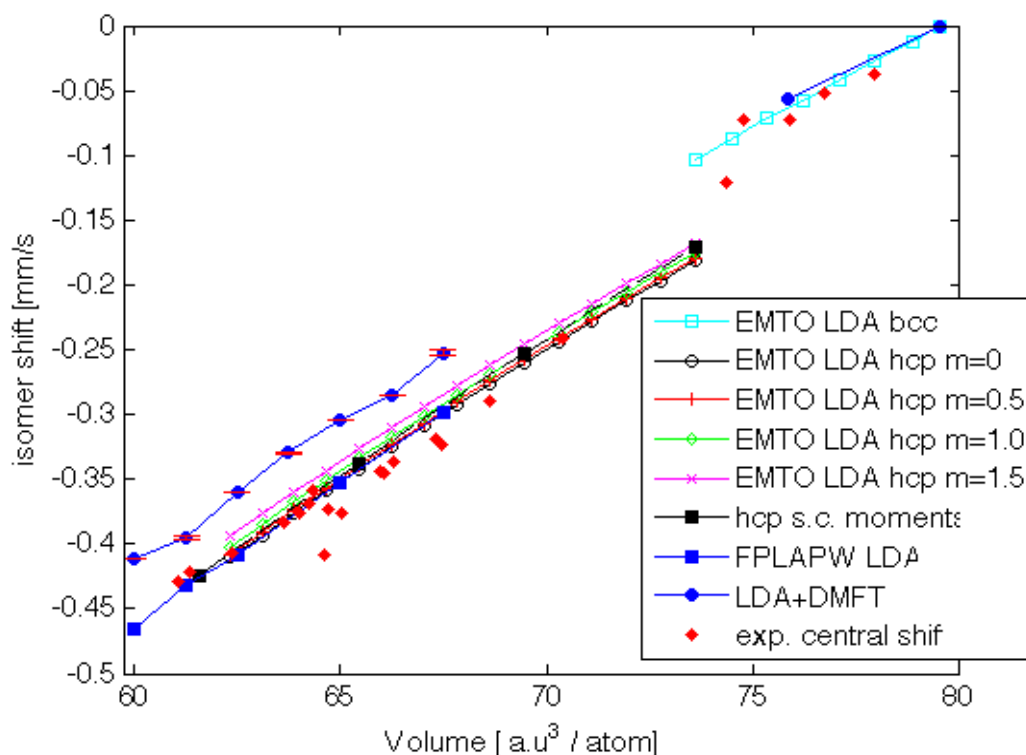
494
495
496   **Fig. S2.2.2** Calculated Mössbauer isomer shifts for pure Fe obtained within different
497   approximations as a function of volume, compared to experimental measurements of the
498   centre shift (red solid diamonds). Results for the *bcc* phase (open cyan squares) are
499   shown as obtained using the EMTO-LDA method. Calculations for the *hcp* phase include
500   a non-magnetic state within the LDA based on the EMTO (open black circles) and
501   FPLAPW methods (blue solid squares), as well as paramagnetic states based on the
502   EMTO method with local magnetic moments 0.5 μ_B (red plus-signs), 1.0 μ_B (green open
503   diamonds), and 1.5 μ_B (pink crosses) and self-consistent moments (Fig. S2.2.1) obtained
504   by spin-fluctuation theory (black squares). We also present results obtained using the
505   LDA+DMFT method (blue filled circles). The error bars correspond to +/- 2 standard
506   deviations of the obtained isomer shift in the LDA+DMFT iterations. All shifts are
507   relative to a reference point at ambient pressure, which was recalculated within all above
508   methods for a correct evaluation of the shifts.
509

510   **References:**

511   [S1]   R. Rüffer and A. I. Chumakov, Hyperfine Interact **97-98**, 589 (1996).

512   [S2]   R. Lübbers, H. F. Grünsteudel, A. I. Chumakov, and G. Wortmann, Science **287**,
513   1250 (2000).

514   [S3]   V. G. Kohn and A. I. Chumakov, Hyperfine Interactions **125**, 205 (2000).

515   [S4]   W. Sturhahn, J. Phys.: Condens. Matter **16**, S497 (2004).

516   [S5]   M. Y. Hu, W. Sturhahn, T. S. Toellner, P. D. Mannheim, E. D. Brown, J. Zhao,
517   and E. E. Alp, Phys. Rev. B **67**, 094304 (2003).

518   [S6]   L. S. Dubrovinsky, S. K. Saxena, F. Tutti, S. Rekhi, and T. LeBehan, Phys. Rev.
519   Lett. **84**, 1720 (2000).

520   [S7]   H.-K. Mao, Y. Wu, L. C. Chen, J. F. Shu, and A. P. Jephcoat, J. Geophys. Res.
521   **95**, 21737 (1990).

522   [S8]   S. D. Jacobsen, C. M. Holl, K. A. Adams, R. A. Fischer, E. S. Martin, C. R.
523   Bina, J.-F. Lin, V. B. Prakapenka, A. Kubo, and P. Dera, American Mineralogist
524   **93**, 1823 (2008).

525   [S9]   J. Rodríguez-Carvajal, Physica B: Condensed Matter **192**, 55 (1993).

526   [S10]   T. J. B. Holland and S. A. T. Redfern, Mineral Mag **61**, 65 (1997).

527   [S11]   S. Ono, T. Kikegawa, N. Hirao, and K. Mibe, American Mineralogist **95**, 880
528   (2010).

529   [S12]   A. Dewaele, P. Loubeyre, F. Occelli, M. Mezouar, P. I. Dorogokupets, and M.
530   Torrent, Phys. Rev. Lett. **97**, 215504 (2006).

531   [S13]   G. Cort, R. D. Taylor, and J. O. Willis, J. Appl. Phys. **53**, 2064 (1982).

532   [S14]   O. Mathon, F. Baudelet, J. Itié, A. Polian, M. d' Astuto, J. Chervin, and S.
533   Pascarelli, Phys. Rev. Lett. **93**, (2004).

534   [S15]   L. Dubrovinsky, N. Dubrovinskaia, O. Narygina, I. Kantor, A. Kuznetzov, V. B.
535   Prakapenka, L. Vitos, B. Johansson, A. S. Mikhaylushkin, S. I. Simak, and I. A.
536   Abrikosov, Science **316**, 1880 (2007).

537   [S16]   C. S. Yoo, J. Akella, A. J. Campbell, H. K. Mao, and R. J. Hemley, Science **270**,
538   1473 (1995).

539   [S17]   M. Aichhorn, L. Pourovskii, V. Vildosola, M. Ferrero, O. Parcollet, T. Miyake,
540   A. Georges, and S. Biermann, Phys. Rev. B **80**, 085101 (2009).

541   [S18]   M. Aichhorn, L. Pourovskii, and A. Georges, Phys. Rev. B **84**, 054529 (2011).

542   [S19]   A. Georges, G. Kotliar, W. Krauth, and M. J. Rozenberg, Rev. Mod. Phys. **68**,
543   13 (1996).

544   [S20]   V. I. Anisimov, A. I. Poteryaev, M. A. Korotin, A. O. Anokhin, and G. Kotliar,
545   J. Phys.: Condens. Matter **9**, 7359 (1997).

546   [S21]   A. I. Lichtenstein and M. I. Katsnelson, Phys. Rev. B **57**, 6884 (1998).

547   [S22]   P. Blaha, K. Schwarz, G. Madsen, D. Kvasnicka, and J. Luitz, *WIEN2k, An*
548   *Augmented Plane Wave + Local Orbitals Program for Calculating Crystal*

549   *Properties* (Techn. Universitat Wien, Wien, Austria, 2002).

550   [S23]   P. Werner, A. Comanac, L. de' Medici, M. Troyer, and A. Millis, Phys. Rev.
551   Lett. **97**, 076405 (2006).

552   [S24]   T. Miyake, F. Aryasetiawan, and M. Imada, Phys. Rev. B **80**, 155134 (2009).

553   [S25]   M. T. Czyzdotyk and G. A. Sawatzky, Phys. Rev. B **49**, 14211 (1994).

554   [S26]   K. S. D. Beach, Cond-mat/0403055 (2004).

555   [S27]   J. A. Moyzis and H. G. Drickamer, Phys. Rev. **171**, 389 (1968).

556   [S28]   D. L. Williamson, S. Bukshpan, and R. Ingalls, Phys. Rev. B **6**, 4194 (1972).

557   [S29]   H. Akai, S. Blügel, R. Zeller, and P. H. Dederichs, Phys. Rev. Lett. **56**, 2407
558   (1986).

559   [S30]   L. Vitos, I. A. Abrikosov, and B. Johansson, Phys. Rev. Lett. **87**, 156401 (2001).

560   [S31]   A. V. Ruban and I. A. Abrikosov, Rep. Prog. Phys. **71**, 046501 (2008).

561   [S32]   S. Fernbach, Rev. Mod. Phys. **30**, 414 (1958).

562   [S33]   B. L. Gyorffy, A. J. Pindor, J. Staunton, G. M. Stocks, and H. Winter, J. Phys. F:
563   Met. Phys. **15**, 1337 (1985).

564   [S34]   A. V. Ruban, S. Khmelevskyi, P. Mohn, and B. Johansson, Phys. Rev. B **75**,
565   054402 (2007).

566   [S35]   W. Potzel, M. Steiner, H. Karzel, W. Schiessl, M. Köfferlein, G. M. Kalvius,
567   and P. Blaha, Phys. Rev. Lett. **74**, 1139 (1995).

568